Axial H-bonding Solvent Controls Inhomogeneous Spectral Broadening, Peripheral H-bonding Solvent Controls Vibronic Broadening: Cresyl Violet in Methanol

Christopher A. Myers, ^{1, a)} Shao-Yu Lu, ^{1, a)} Sapana Shedge, ¹ Arthur Pyuskulyan, ¹ Katherine Donahoe, ¹ Ajay Khanna, ¹ Liang Shi, ^{1, b)} and Christine M. Isborn ^{1, c)} Department of Chemistry and Biochemistry, University of California Merced, Merced, California 95343, USA

The dynamics of the nuclei of both chromophore and its condensed phase environment control many spectral features, including the vibronic and inhomogeneous broadening present in spectral lineshapes. For the cresyl violet chromophore in methanol, we here analyze and isolate the effect of specific chromophore-solvent interactions on simulated spectral densities, reorganization energies, and linear absorption spectra. Employing both force field and ab initio molecular dynamics trajectories along with the inclusion of only certain solvent molecules in the excited state calculations, we determine that the methanol molecules axial to the chromophore are responsible for the majority of the inhomogeneous broadening, with a single methanol molecule that forms an axial hydrogen bond dominating the response. The strong peripheral hydrogen bonds do not contribute to spectral broadening, as they are very stable throughout the dynamics and do not lead to increased energy gap fluctuations. We also find that treating the strong peripheral hydrogen bonds as molecular mechanical point charges during the molecular dynamics simulation underestimates the vibronic coupling. Including these peripheral hydrogen bonding methanol molecules in the quantum mechanical region in a geometry optimization increases the vibronic coupling, suggesting that a more advanced treatment of these strongly interacting solvent molecules during the molecular dynamics trajectory may be necessary to capture the full vibronic spectral broadening.

I. INTRODUCTION

Simulating accurate condensed phase spectral lineshapes requires the inclusion of both vibronic and solvent effects. Such effects contribute to spectral width. as well as shape, with vibronic transitions often causing a high energy tail in absorption spectra and solvent effects often leading to inhomogeneous broadening. Although this inhomogeneous broadening is generally accounted for with a phenomenological broadening parameter, it is specific interactions between a chromophore and the solvent, such as solvent hydrogen bonding and dipole-dipole interactions, that lead to the energy fluctuations responsible for inhomogeneous spectral broadening. Sampling from an ensemble of independent chromophore-solvent nuclear configurations can capture environmental effects within a nuclear ensemble approach to simulating the lineshape, 1-4 but this nuclear ensemble approach lacks vibronic transitions. The vibronic effects on a spectrum can be accounted for with a Franck-Condon calculation, 5-11 often performed within the harmonic approximation with an implicit polarizable continuum model for the environment. 12–16

Alternative methods can simultaneously include vibronic and specific environmental effects. Recent work by some of the authors shows how to combine the Franck-Condon approach for the chromophore with an ensemble

ium betaine dye molecule revealed solvent-induced spec-

tral narrowing due to the solute vibrational modes com-

Specific solvent interactions are known to cause spec-

of explicit solvent-chromophore configurations sampled from molecular dynamics (MD). 17-20 A method similar in spirit to this is the recently developed adiabatic MD generalized vertical Hessian approach, is based on partitioning the nuclear motions into soft and stiff vibrational modes, where the stiff modes contribute to the vibronic spectrum and the soft modes are treated classically through MD conformational sampling.²¹ An alternative approach is to follow the dynamics of the chromophore and solvent by saving an MD trajectory of chromophore-solvent configurations for the computation of energy gaps between the ground and excited states. The energy gap correlation function can then be used to compute the spectral density, 22 which shows how vibrational modes couple to the optical excitation and the resulting optical spectra, such as the resonance Raman spectrum and the absorption spectrum. $^{14,18,20,23-32}$ This trajectory-based approach is able to capture both vibronic effects and specific environmental effects on the optical spectrum on an equal footing as nuclear degrees of freedom of both the chromophore and the environment are taken into consideration at the level of the energy gap calculation.

tral changes. The formation of hydrogen bonds (H-bonds) between chromophore and solvent can blue-shift or red-shift peaks in the optical spectrum.^{33,34} Recent studies have examined how H-bonding of water to flavin affects the vibrational frequencies³⁵ and band intensities.³⁶ Analysis of the effects of water solvent molecules on the vibronic spectrum of an oxyguinolin-

a) These authors contributed equally to this work.

b) Electronic mail: lshi4@ucmerced.edu

c) Electronic mail: cisborn@ucmerced.edu

bined with broadening of the spectra due to vibronic progressions along the solute/solvent H-bonds.³⁷ One advantage of a trajectory-based approach is that changes in excitation energy and energy fluctuations can be connected to specific chromophore-solvent interactions and even solvent dynamics. For example, by careful analysis of the trajectory, for the anionic chromophore of photoactive yellow protein, deprotonated trans-thiophenyl-p-coumarate (pCT⁻), some of the authors showed that low-frequency motions of the chromophore with the surrounding solvent led to spectral broadening, and coupling of the high-frequency motion of the C=O stretch to solvent led to increased vibronic coupling.^{29,38}

To fully realize the aforementioned advantages of the trajectory-based approach, we need an accurate description of both the chromophore and chromophore-solvent interactions, as well as a reliable approach for the computation of electronic excitation in the presence of solvent. For the latter, time-dependent density functional theory (TDDFT) has been the main workhorse with its modest computational cost and reasonable accuracy, and in our previous work, we have suggested guidelines for the use of TDDFT in excited state calculations of condensed phase systems. ^{19,29,39–41} For the former issue, ab initio molecular dynamics (AIMD) with density functional theory (DFT) offers quantum-chemical accuracy at a high computational cost that limits the time scale for sampling configuration space, whereas more affordable force-field-based MD (FFMD), usually with empirical parameters, may suffer from poor descriptions of the chromophore or of specific chromophore-solvent interactions. Furthermore, it has been shown that a mismatch between the potential used for the MD simulation and the excitation energy calculations (e.g., using FFMD for the trajectory and TDDFT for excited state computation) introduces artifacts to the computed spectral density. 23-26,42 It is thus desirable to either use the same quantum chemical protocol (i.e., functional, basis set, and solvent treatment) for MD simulation and excited state calculations (e.g. with AIMD and TDDFT employing the same functional), or to parametrize the force field (FF) using the same quantum chemical protocol as used for the excited state calculation to minimize the mismatch. Recent advances in ab initio based FF parametrization provide a promising way forward, with many approaches designed to reproduce quantum mechanical (QM) results. 43-52 One such method that derives system-specific FF parameters directly from QM calculations, including the molecular Hessian and density based charges, is the QUantum mechanical BEspoke Kit (QUBEkit). 53,54

In this work, for the cationic cresyl violet (CV^+) chromophore in methanol, we parametrize custom force fields and perform both FFMD and quantum-mechanics/molecular-mechanics (QM/MM) AIMD simulations, followed by QM/MM TDDFT excited state calculations, to simulate its resonance Raman and UV-Vis absorption spectra. The CV^+ chromophore, also known

as oxazine-9, is a member of the family of organic cationic oxazine dyes widely used as both laser dyes and fluorescence sensors. 55,56 CV⁺ is sensitive to the local hydrogen bonding and dielectric environment, and the absorption and fluorescence, resonance Raman, and nonlinear optical spectra have been measured experimentally in a variety of solvent environments. $^{56-63}$ The absorption spectrum of CV⁺ in methanol is broad, with a maximum at 2.1 eV and a shoulder at 2.25 eV. 58,63 This shoulder could be due to a higher lying excited state, but previous studies suggest it is from a vibronic transition between the ground state and bright S_1 state. 56,61,64 Here we analyze the environmental and vibronic contributions to the computed linear absorption spectrum using the trajectorybased approach. We find that different hydrogen-bonding solvent molecules play different roles in shaping the absorption spectrum, demonstrating the importance of accurate treatment of chromophore-solvent interactions in both MD simulations and TDDFT calculations.

II. THEORY

We here present the theoretical expressions used to simulate the spectral densities, resonance Raman, and absorption spectra from MD simulations. We assume that our chromophore is well-represented by a two-level system consisting of the ground and first excited electronic state. The absorbance, $\sigma(\omega)$, of a chromophore in the impulsive limit is then given by

$$\sigma(\omega) \propto \omega \int_{-\infty}^{\infty} dt \, \chi(t) e^{i\omega t},$$
 (1)

where $\chi(t)$ is the linear response function. The key to formulating the approximate approaches for linear spectroscopy from an MD trajectory is to express the linear response function in terms of a cumulant expansion for the ensemble average of the time-ordered exponential.²² The linear response function, within the Condon approximation, can then be written as²²

$$\chi(t) = |\boldsymbol{\mu}_{\text{eg}}|^2 e^{-i\bar{\omega}_{\text{eg}}t} \exp\left[-\sum_{n=2}^{\infty} g_n(t)\right],$$

where $\bar{\omega}_{\rm eg} = \langle U(t) \rangle$ is the thermal average of the energy gap operator U connecting the electronic ground state g to the excited state e, $\mu_{\rm eg}$ is the transition dipole moment between these two states, which is taken as a constant within the Condon approximation, and $g_n(t)$ is the n^{th} order cumulant function. Atomic units are used throughout these expressions, unless stated otherwise. If the energy fluctuations of the system follow Gaussian statistics, truncation of the cumulant expansion is exact at second order. The absorption is then determined completely by the second-order cumulant, $g_2(t)$, which can be eval-

uated as^{22}

$$g_2(t) = \frac{1}{\pi} \int_0^\infty d\omega \, \frac{J(\omega)}{\omega^2} \left[\coth\left(\frac{\beta\omega}{2}\right) \left[1 - \cos(\omega t)\right] + i\left[\sin(\omega t) - \omega t\right] \right]. \tag{2}$$

The spectral density, $J(\omega)$, requires the evaluation of the energy gap fluctuation quantum time correlation function (TCF), which is generally not accessible for any realistic system. Phenomenological corrections have been devised to approximate the quantum TCF with its classical counterpart. A popular choice in the context of electronic spectroscopy is the harmonic quantum correction factor (QCF), which leads to the approximate expression for $J(\omega)$ as 70

$$J(\omega) = \Theta(\omega) \frac{\beta \omega}{2} \int_{-\infty}^{\infty} dt \ e^{i\omega t} \ C_{\rm cl}(t), \tag{3}$$

where $\Theta(\omega)$ is the Heaviside step function. The classical TCF, $C_{\rm cl}(t)$, of the vertical excitation energy (VEE) fluctuations, can be obtained from computing excitation energies for a series of time-correlated snapshots of nuclear configurations generated from an MD trajectory, $^{14,27,71-75}$ which we here denote as U(t), as

$$C_{\rm cl}(t) = \langle \delta U(t) \delta U(0) \rangle_{\rm cl},$$
 (4)

where $\delta U(t) = U(t) - \bar{\omega}_{\rm eg}$ is the energy gap fluctuation, and the angular brackets with the subscript "cl" indicate a classical equilibrium ensemble average. The harmonic QCF is known to be exact for the TCF of an operator that linearly depends on the harmonic vibrational coordinates, ⁶⁷ which also makes the truncation of the cumulant expansion at second order exact. ²² The spectral density measures the coupling strength between the electronic excitation and nuclear motions. Another property that quantitatively measures the coupling between the electronic transition and nuclear motion is the reorganization energy, which is related to spectral density as ²²

$$\lambda = \frac{1}{\pi} \int_0^\infty \frac{J(\omega)}{\omega} d\omega. \tag{5}$$

One experimental observable that can probe the spectral density directly is resonance Raman. Within the transform theory of Raman scattering, the first order resonance Raman intensity for the displaced harmonic oscillators with the same vibrational frequencies on the ground and excited electronic state is approximately proportional to the spectral density. The approximations invoked include the Condon approximation and the neglect of the average thermal population of vibrational modes, which are valid for our system and the frequency window of interest.

Different nuclear motions play different roles in shaping the absorption spectrum: the high-frequency modes

of the spectral density, often involving the intramolecular vibrations of the chromophore, can produce a vibronic Franck-Condon progression and vibrational coherences, whereas the low-frequency modes due to the collective motions of the chromophore and its local environment (e.g. solvent molecules) inhomogeneously broaden the spectrum. Separation of the high- and low-frequency contributions to the absorption spectrum enable the separate analysis of the inhomogeneous broadening and vibronic contributions to spectral lineshapes.

We define the spectral density from the low-frequency modes as

$$J_{\rm LF}(\omega) = \frac{1}{2} \left[1 - \operatorname{erf}\left(\frac{\omega - \omega_c}{\sigma}\right) \right] J(\omega), \tag{6}$$

where $\operatorname{erf}(x)$ is the error function and ω_c is a parameter for the cutoff frequency and we choose $\omega_c = 200 \, \mathrm{cm}^{-1}$ as $k_B T$ is about 200 cm^{-1} at the ambient temperature. The parameter σ determines how quickly the high-frequency modes are turned off, and is taken to be $2 \, \mathrm{cm}^{-1}$, which ensures a sharp yet continuous turnoff of the high-frequency modes. Note that the choice of the values for ω_c and σ is not unambiguous. With the low-frequency spectral density, $J_{\mathrm{LF}}(\omega)$, we compute the absorption spectrum and reorganization energy (λ_{LF}) from the low-frequency nuclear motions in the MD trajectory. The high-frequency spectral density is determined by applying an error function with the same cutoff frequency,

$$J_{\rm HF}(\omega) = \frac{1}{2} \left[1 + \operatorname{erf}\left(\frac{\omega - \omega_c}{\sigma}\right) \right] J(\omega).$$
 (7)

III. COMPUTATIONAL DETAILS

A. Choice of density functional for QM/MM AIMD and QM/MM TDDFT excited state calculations

DFT is used to treat the chromophore during QM/MM simulations and to parametrize the force field for classical MD, whereas TDDFT is used to model the excited states as discussed below. The excitation energies depend strongly on the degree of Hartree-Fock (HF) exact exchange in the density functional, with more HF exact exchange generally leading to higher excitation energies. In a previous study by Kostiukov that surveyed the performance of forty hybrid density functionals for simulating the absorption spectrum of the aqueously solvated cresyl violet cation, the range-separated CAM-B3LYP functional that includes a larger percentage of HF exact exchange at long-range was one of the most accurate when comparing the energies of the simulated and experimental vibronic maxima, along with M06-2X and long-range corrected ω -B97XD functionals.⁶⁴ The vibronic spectra generated from this same study produced a vibronic shoulder weaker than in the experimental spectrum, with the author noting that spectra generated using all 40 functionals had nearly the same shape. Indeed,

our benchmark calculations of Franck-Condon vibronic spectra for CV⁺ in a polarizable continuum model for methanol (see Figure S1) show very similar vibronic lineshapes for CAM-B3LYP, M06-2X, and ω -B97XD, with M06-2X producing a slightly more narrow spectrum and ω -B97XD producing a slightly broader spectrum than CAM-B3LYP. We also show the vibronic spectrum generated by the LC- ω HPBE functional, which is broader than the other spectra, likely due to the larger value of the range-separation parameter ($\omega=0.40$ for LC- ω HPBE, $\omega=0.20$ for ω -B97XD). Because the CAM-B3LYP functional has yielded accurate vibronic spectral shapes in studies of other systems, ^{19,80,81} we here use the CAM-B3LYP functional.

B. Force field parametrization and solvation

We here use the QUBEKit^{53,54} code (version 2.6.3) and protocol to parametrize a bespoke force field for the CV⁺ chromophore using ab initio data obtained with the range-separated hybrid CAM-B3LYP functional and 6-31G(d) basis set. QUBEKit interfaces with the Gaussian electronic structure code to obtain the necessary optimized structures, frequencies, torsion scans of the potential energy surface, and other properties. The ground state optimized structures and frequencies were obtained in vacuum, along with the torsion scan of the potential to fit the dihedral force constants. A QUBEKit force field was parameterized for methanol using the same procedure.

A key element of the force field accuracy is determined by the chromophore charges. Using the ground state optimized structure, the ground state wave function computed with a polarizable continuum model of methanol was used to obtain the DDEC6 partial atomic charges with the chargemol program.^{82,83} The CAM-B3LYP/6-31G(d) predicted ground state dipole moment of 5.4 D increases by 1.2 D in the excited state to a value of 6.6 D, with this increase a bit smaller than the 1.5-2.1 D measured in experiments. 61,84 We find that the DDEC6 ground state dipole moment is slightly smaller than the QM value, at 4.3 D. In contrast, charges computed with the Merz-Kollman model. 85–87 which we later use to reparametrize the force field as described in the next section, agree with the QM dipole moment. The cresyl violate molecule was solvated in a 32 Å radius sphere of methanol, with the same procedure followed with QUBEKit to generate a ground state force field for the methanol molecule.

The Lennard-Jones (LJ) parameters in the QUBEKit force field were derived directly from the quantum mechanically computed electron densities using the atoms-in-molecule (AIM) approach, ⁸⁸ ensuring that these parameters are specific to the chemical environment of each atom within the molecule. The LJ parameters for interactions between different atoms were obtained using the Lorentz-Berthelot combination rule. Once the parame-

terization was completed, the resulting force field files were converted to those compatible with AMBER using the ParmEd Tool.⁸⁹ We refer interested readers to Ref. 88 for details, and the AMBER input files for running MD simulations with the parameterized QUBEKit force field are provided in the SI.

We also used the Generalized Amber Force Field (GAFF)⁹⁰ for some initial MD simulations, but did not perform in depth analysis as the vibrational modes of the chromophore were not as accurate as those from QUBEKit (see SI discussion and Figure S2).

C. Force field molecular dynamics

The QUBEKit FFMD simulations were run using the AMBER program. 91,92 Energy minimization for the droplets was first performed using 50 steps of a steepest descent algorithm, followed by 950 steps of conjugate gradient algorithm. Following the energy minimization, the system was slowly heated from 10 to 300 K over a period of 40 ps, using the Langevin thermostat^{93,94} with a friction coefficient of 5 ps⁻¹. After heating, a short equilibration was performed at 300 K using the Langevin thermostat for 10 ps followed by 50 ps equilibration using the Berendsen⁹⁵ thermostat with a coupling time constant of 1 ps. The production run was performed in the NVT ensemble at 300 K. The time step was 0.5 fs, and the center of mass motion was removed every 2000 steps. The production simulation was run for 60 ps and configurations were saved every 4 fs as snapshots for further analysis.

As described in the results section, a longer 10 ns simulation was also run with a modified version of the QUBEKit derived FF using Merz-Kollman charges, where we here used the OpenMM 8.0 simulation toolkit. 96 The cresyl violet molecule was placed in a $50\,$ Å cubic solvation box of methanol and minimized with an L-BFGS algorithm using the default OpenMM criteria for convergence. The system temperature was then equilibrated to 300 K using a Langevin thermostat for 500 ps with a 5 ps⁻¹ friction coefficient. A subsequent 500 ps pressure equilibration was also performed using a Monte-Carlo barostat at 1 bar combined with a 1 ps⁻¹ Nosé-Hoover middle integrator. 97 The production NVT simulation was run with the Nosé-Hoover thermostat for 10 ns and uncorrelated configurations were saved every 1 ps for analysis. A shorter 60 ps simulation was also performed for comparison to the 60 ps QM/MM AIMD simulations (see below) and was initialized from a simulation frame obtained from the 10 ns production run. All equilibration and production simulations used a time step of 0.5 fs under the CUDA platform of OpenMM. OpenMM files needed to run this revised force field molecular dynamics trajectory are provided in the SI.

D. QM/MM ab initio molecular dynamics

The QM/MM AIMD simulations were run using the AMBER-TeraChem interface, 39 where CV⁺ was treated at the QM level with CAM-B3LYP/6-31G(d) and methanol was treated as MM molecules using the QUBEKit potential. The fixed MM point charges of the surrounding methanol moelcules were electrostatically embedded into the QM Hamiltonian, allowing the QM electron density to be polarized by the solvent environment. Lennard-Jones interactions between the chromophore and the methanol from the QUBEKit force field were also included in the total energy of the system. Starting from the final time step of the classical field field equilibration, the QM/MM AIMD were run for 20 ps to equilibrate the transfer of the chromophore from a classical to a QM potential energy surface (see Figure S3). The production QM/MM MD simulation ran for 60 ps at fixed NVT using a Berendsen thermostat with a 1 ps time constant.

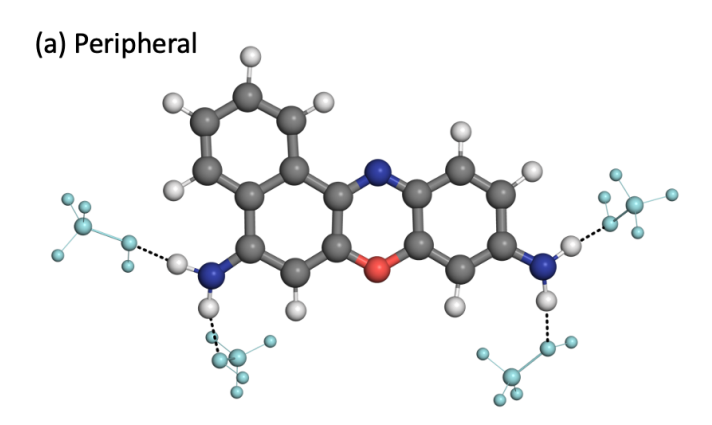
E. QM/MM excited state calculations

Snapshots of solvated CV^+ generated from both the FFMD and QM/MM AIMD simulations were used for the calculation of QM/MM excitation energies with TDDFT using CAM-B3LYP/ 6-31G(d) within the Tamm-Dancoff approximation (TDA). 98 The MM point charges of the solvent were electrostatically embedded in the QM Hamiltonian. The TeraChem GPU accelerated electronic structure package^{99,100} was used for all vertical excitation energy calculations. The resulting excitation energies were then used to build the energy gap correlation function, employed in Eq. 4, for simulation of the spectral density and linear absorption spectra. No mixing between the bright S₁ and dark S₂ state was observed along the trajectory, see Figure S4. All linear spectra and spectral densities were calculated using the MolSpeckPy spectroscopy package. 101 To obtain a wellbehaved Fourier transform, the classical time correlation function was multiplied by an exponential damping function with a decay time constant of 500 fs.

F. Peripheral and axial chromophore-solvent interactions

We classify two types of chromophore-solvent interactions between CV^+ and methanol. The first is where the amine groups of CV^+ act as H-bond donors, forming four peripheral H-bonds with the oxygen of methanol solvent molecules. The second is for the methanol solvent molecules interacting with the π -system of CV^+ above and below the axial region of the plane of the chromophore, see Figure 1. These chromophore-solvent interactions lead to two different kinds of hydrogen bonds that we discuss herein, (1) peripheral H-bonds and (2)

axial H-bonds where the axial methanol molecules donate their OH group to the amine group of $\mathrm{CV^+}$, where now $\mathrm{CV^+}$ acts as an H-bond acceptor. We generously define a hydrogen bond as forming if the donor-acceptor distance between heavy atoms is within 3.2 Å of each other, the distance between the hydrogen and its accepting heavy atom is within 2.2Å of each other, and the donor-hydrogen-acceptor angle is greater than or equal to 110 degrees.



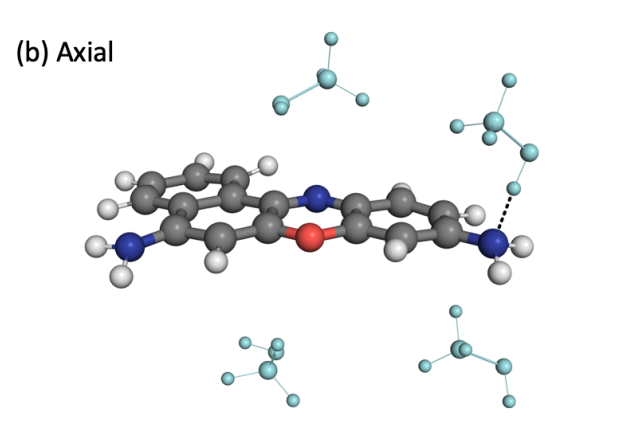


FIG. 1. Chromophore-solvent interactions between cresyl violet and methanol are classified into two types. (a) Amine groups act as H-bond donors, forming four peripheral H-bonds with the oxygen of methanol solvent molecules. (b) The four closest solvent molecules in what we call the axial region of solvation, where we here highlight the formation of an axial H-bond between methanol and the amine group of CV⁺.

IV. RESULTS AND DISCUSSION

A. Analysis of chromophore-solvent interactions

Condensed phase MD simulations capture explicit interactions between the chromophore and surrounding solvent molecules that directly affect the optical spectroscopy. In this section we analyze those interactions before moving on to analyzing their effects on optical spectra.

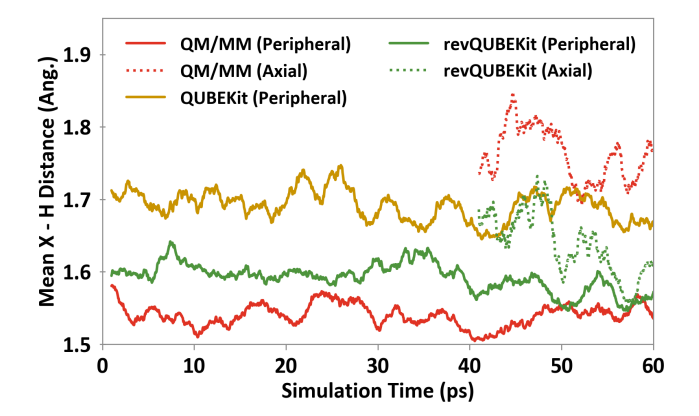


FIG. 2. Average H-bond distance for cresyl violet and methanol for peripheral (solid) and axial (dash) H-bonds. Peripheral H-bond distances are averaged over four H-bonds, axial H-bond distance is for a single H-bond. RevQUBEKit trajectory simulation start time is chosen to align axial H-bonding events. H-bond distance profiles are smoothed by averaging over all bonds formed within 2 ps of the MD time step (1 ps before and after this time).

First, we compare the H-bonding between CV⁺ and methanol obtained from 60 ps of QM/MM AIMD and from 60 ps of QUBEKit FFMD trajectories. The two amine groups of CV⁺ are the sites of H-bonding with methanol solvent molecules (note that no H-bonding at the oxygen or nitrogen of the center ring was observed in any of the MD simulations). In both trajectories, the hydrogens of the amine groups form strong H-bonds to the oxygen of the methanol molecules that are peripheral to the chromophore. Analysis of this peripheral Hbonding shows a stable H-bond formed to all four amine hydrogens, with the identity of the H-bonding methanol molecule not changing throughout the 60 ps trajectory. The average distance of the peripheral H-bond (the distance between the amine hydrogen and the methanol oxygen), shown over time in Figure 2, is 1.54 ± 0.13 Å for QM/MM AIMD compared to 1.70 ± 0.17 Å for QUBEKit FFMD, indicating a stronger bond with the QM/MM model compared to the QUBEKit FF MM only model.

In the QM/MM AIMD trajectory, we observe the formation of an axial H-bond with one of the amine groups just after 40 ps, where the amine accepts an H-bond from a methanol molecule. This QM/MM axial H-bond distance (the distance between the amine nitrogen and the hydroxyl hydrogen of methanol) is longer than the peripheral H-bonds, indicating a weaker H-bonding interaction than when the amine acts as an H-bond donor. Analysis of the QUBEKit FFMD trajectory showed no such axial H-bond formation over the course of 60 ps. Wondering if this was just a question of sampling and if we would see the formation of the axial H-bond if we ran a longer trajectory, we extended the QUBEKit trajectory to 10 ns, but found no axial H-bond formation.

Further speculating if differences in polarization could

be the cause of this disparate H-bonding behavior, to analyze the polarization within the QM/MM model we computed the partial atomic charges of CV⁺ surrounded by the explicit methanol MM point charges. We averaged over 21 snapshots that included the axial H-bond, comparing these values to the original charges computed with implicit solvent. The axial H-bonding interaction, along with the point charges of the explicit solvent environment, leads to more significant polarization of CV⁺. with an increase in magnitude of the H-bonding nitrogen charge of 0.114e. To better understand the origin of this increased polarization, we analyzed the electric field at the CV⁺ nitrogen due to the surrounding solvent environment, and found a substantial increase in the electric field upon formation of the axial bond, with the majority of the electric field being aligned with the π -system of the chromophore, see Figure S5.

We repeated this same implicit and explicit partial atomic charge computation with the Merz-Kollman (MK) charge method⁸⁵ that is known to provide an accurate polarization description.^{86,87} With the MK charge method, we found a further increase in polarization, with an increase in magnitude of the nitrogen charge of 0.438e compared to the original DDEC6 charge method for implicit solvent. A table of both the DDEC6 and MK charges is given in the SI, Table S1 and accompanying Figures S6 and S7.

We next examined the potential energy surface generated from moving both peripheral and axial methanol H-bonds away from CV⁺ at the site of the polarized nitrogen. We computed the energies along the H-bond distance coordinate, keeping the remaining solvent fixed. The potentials were generated using (1) the original QUBEKit DDEC6 charges for CV⁺, (2) the new MK charges for CV⁺ from explicit solvent polarization, which we use to generate a revised QUBEKit force field that we call revQUBEKit, (3) the same electronic structure method as was used in the QM/MM AIMD simulation, with CV⁺ treated with CAM-B3LYP/6-31G(d) and all remaining solvent as MM, and (4) CV⁺ and the H-bonding methanol molecule treated with CAM-B3LYP/6-31G(d) and all remaining solvent as MM, denoted as QM-QM/MM, see Figure 3. For the peripheral H-bond, the QM/MM, QUBEKit, and revQUBEKit methods all share a potential minima at 1.6 Å. The strength of the H-bonds fall between 10.5 and 12.2 kcal/mol at their minimum interaction distances. For the QM treatment of methanol, the depth of the potential well is similar, but the minimum of the well is at a larger distance of 1.9 Å. For the axial H-bond, the original DDEC6 implicit solvent QUBEKit charges produce a very weak potential, with the H-bond only yielding \sim 2 kcal/mol of stabilization. In contrast, the QM-MM treatment of the chromophore-methanol interaction, the QM-QM treatment of the chromophore-methanol interaction, along with the revQUBEKit force field generated with the MK charges from explicit solvent configurations, yields 7-8 kcal/mol of stabilization upon forming the ax-

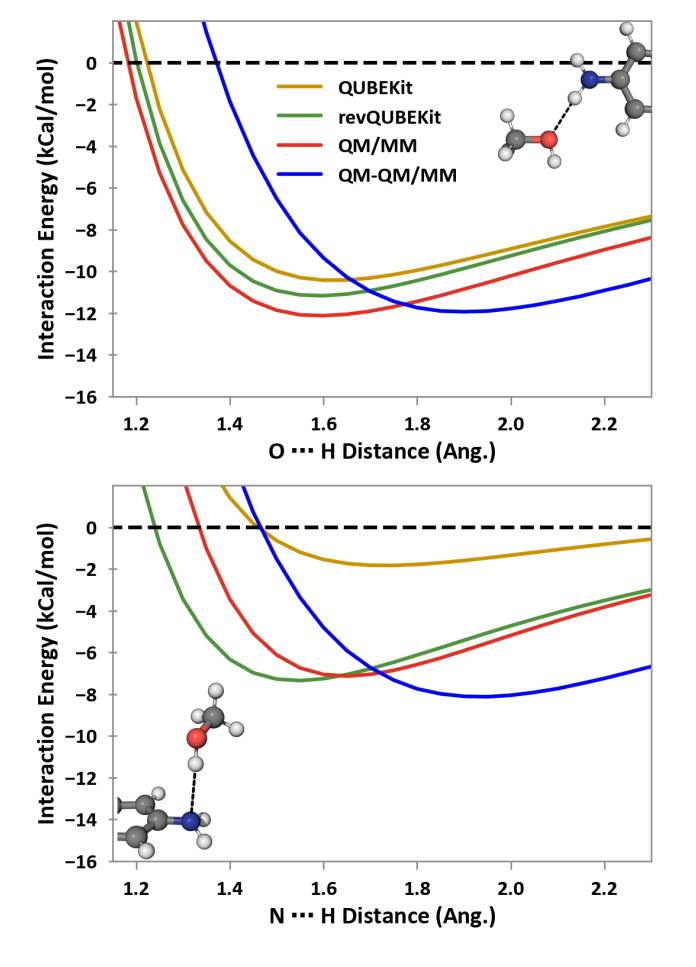


FIG. 3. Interaction energies between cresyl violet and a single methanol solvent molecule that forms a peripheral H-bond at the amine group (top) and an axial H-bond at the amine group (bottom). For the QM/MM model, CV⁺ is treated as QM and all solvent as MM. For the QM-QM/MM model, CV⁺ is treated as QM and the H-bonding methanol is treated as QM, with all other solvent as MM.

ial H-bond. The energy minima for revQUBEKit and CAM-B3LYP with MM solvent are at 1.6 and 1.7 Å distances between the nitrogen and the hydrogen, respectively, with the QM solvent having a minimum at 1.9 Å. The agreement between revQUBEKit and QM/MM in the repulsive region of the potential is less satisfactory. but its impact on MD simulations is expected to be small as the mean N—H distance for the axial H-bond, shown in Figure 2, is always above 1.5 Åfor both revQUBEKit and QM/MM trajectories. The discrepancy between the revQUBEKit, QM/MM, and QM-QM/MM potentials likely is due to the interaction of the methanol with the π cloud of the chromophore, which is captured differently with each method. Overall, these potentials show that the MK charges generated from explicit solvent snapshtos used for revQUBEKit improved the agreement with the QM/MM electronic structure method used for the QM/MM AIMD simulation, but also suggest that a QM

treatment of the solvent would lead to similar energetics but larger H-bonding distances.

With the MK charges generated from explicit solvent QM/MM AIMD snapshots validated against the QM/MM potential, as well as having a dipole moment in better agreement with the DFT computed value (See Table S2), we then ran an FFMD trajectory with this new revQUBEKit FF. The resulting H-bonding distances from 60 ps of the trajectory are shown in Figure 2. The revQUBEKit FF produces average peripheral H-bond distances $(1.59 \pm 0.14 \text{ Å})$ that are in better agreement with the QM/MM values $(1.53 \pm 0.13 \text{ Å})$ compared to the original QUBEKit FF distances (1.70 \pm 0.17 Å). A more significant change, however, is that now an axial Hbond is formed at the CV⁺ amine site due to increased polarization of the nitrogen. The average H-bond length is shorter for revQUBEKit $(1.65 \pm 0.20 \text{ Å})$ compared to QM/MM $(1.74 \pm 0.16 \text{ Å})$, in agreement with the minima in the potential shown in Figure 3b. With the computational efficiency of the force field, we are easily able to run a longer trajectory of 10 ns to allow for extended analysis of the axial H-bond dynamics (see SI, Figure S8). Over the course of the 10 ns trajectory, we observe many axial H-bonding interactions at the polarized nitrogen site, with an average H-bond lifetime duration of 40. ps and an upper and lower quartile of 8 ps and 44 ps, respectively (see the SI for details).

We next examine how these differing Hamiltonians and their ability to capture specific chromophore-solvent interactions affect the resulting spectral properties.

B. Comparison of QM/MM and force field models for trajectory based optical spectra

We here validate the vibrational degrees of freedom of the $\mathrm{CV^+}$ chromophore and their couplings with the electronic excitation within our MD trajectories by comparison to experimental resonance Raman before analyzing the computed spectral densities and optical spectra.

The resonance Raman spectrum can be compared to the computed spectral density. In Figure 4, the simulated spectral densities for CV⁺ in methanol are compared to the experimental resonance Raman spectrum that is given from 300-900 cm⁻¹ in Ref 102. We see that the main peak in this spectral window at 600 cm⁻¹ corresponding to the motion of the center oxazine ring is accurately captured by QM/MM, QUBEKit, and revQUBEKit MD. Smaller peaks at $\sim 530 \, \mathrm{cm}^{-1}$ and ~ 850 cm⁻¹, corresponding to a combination of NH₂ and C-H twisting motion and C-H in phase wagging motion, ⁵⁵ respectively, are well-captured by QM/MM AIMD, but less accurately simulated by QUBEKit and revQUBEKit FFMD. In sum, we observe that the QM/MM AIMD vields fairly good agreement with the vibrational frequencies measured for CV⁺ in methanol, with QUBEKit and revQUBEKit FFMD also providing satisfactory results. This good agreement testifies to the high quality of

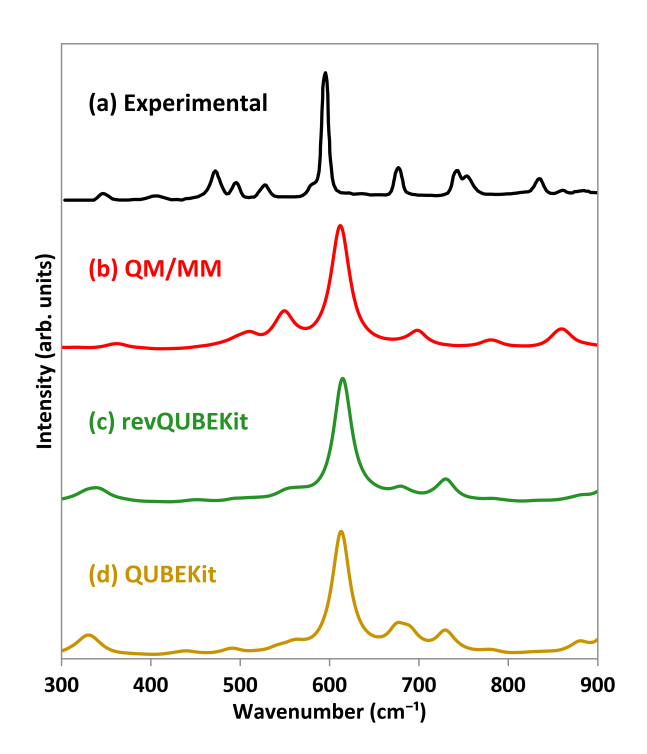


FIG. 4. The top black curve shows the experimental resonance Raman spectrum obtained from Ref. 102, compared to the simulated spectral density of CV^+ in methanol obtained with different MD methods.

our computed spectral densities, at least in the frequency window of $300-900 \text{ cm}^{-1}$.

The spectral density indicates how strongly vibrational degrees of freedom of the chromophore and solvent couple to the bright optical S₁ transition. In Figure 5a we compare the QM/MM AIMD trajectory results with those from the QUBEKit and revQUBEKit FFMD trajectories, with all trajectories sampled for the 60 ps shown in Figure 2. All trajectories show the dominant peak at 600 cm⁻¹, with revQUBEKit giving the highest intensity and QM/MM giving the lowest intensity. Both QUBEKit and revQUBEKit give medium intensity peaks in the range from 600-1300 cm⁻¹, whereas QM/MM produces peaks with relatively smaller intensity in this range. At 1400 cm⁻¹ the QM/MM peaks increase in intensity, and the QUBEKit trajectories produce a peak at $\sim 1600 \text{ cm}^{-1}$, which is of similar intensity as the 600 cm^{-1} peak. Overall, the QUBEKit and revQUBEKit trajectories produce spectral density peaks with higher intensity for these higher frequency chromophore degrees of freedom compared to QM/MM, which we expect to lead to more vibronic structure in the optical spectrum for the FF methods.

The low-frequency region of the spectral density, shown as an inset in Figure 5a, is dominated by the slower solvent degrees of freedom and is responsible for the inhomogeneous broadening in the optical spectrum. Here we see that the QUBEKit trajectory, with no ax-

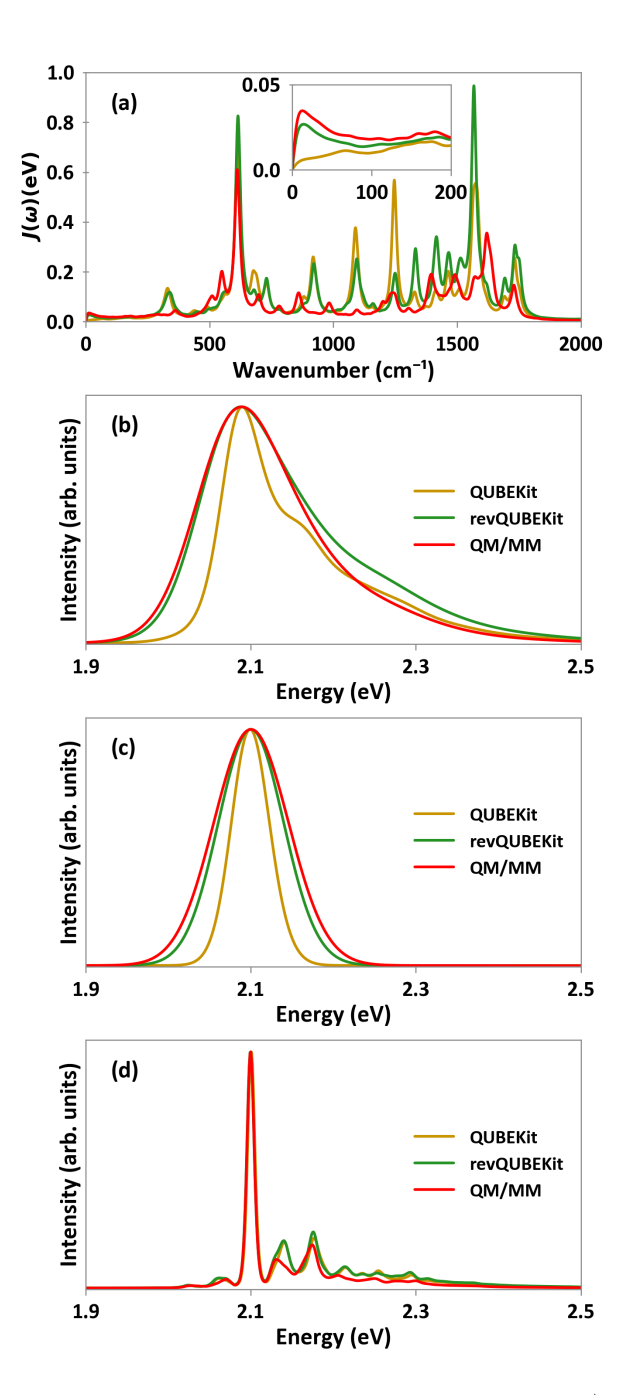


FIG. 5. (a) Computed spectral density $J(\omega)$ for CV^+ in methanol for 60 ps trajectories, (b) corresponding linear absorption spectrum for CV^+ in methanol obtained with different MD methods, (c) linear absorption spectra where only the low frequency (0 - 200 cm⁻¹) and (d) linear absorption spectra where only the high frequency (> 200 cm⁻¹) contributions from the spectral density are considered.

ial H-bonding, produces significantly less intensity in the low-frequency region, suggesting weaker coupling of CV⁺ to the solvent environment. Notably, the revQUBEKit trajectory produces an increase in intensity, with low-frequency results that align fairly well with the QM/MM trajectory. We hypothesize that the increased intensity

for both the QM/MM and the revQUBEK it trajectories is due to the axial H-bond and the strong electric field generated that is aligned with the π -system of the chromophore.

To further quantify how strongly the nuclear degrees of freedom of the chromophore and solvent couple to the electronic transition, we integrated the spectral density to produce the reorganization energy, λ , as given in Eq. 5, and partitioned it into the contributions from the low- and high-frequency regions of the spectral density: the low-frequency reorganization energy, $\lambda_{\rm LF}$, was computed by integrating $J_{LF}(\omega)$ (Eq. 6), and the highfrequency contribution, $\lambda_{\rm HF}$, was simply taken as the difference between λ and $\lambda_{\rm LF}$. As shown in the top part of Table I, QUBEKit (0.011 eV) significantly underestimates λ_{LF} compared to that from QM/MM (0.040 eV), whereas revQUBEKit (0.030 eV) improves the agreement substantially, consistent with our observation of the lowfrequency region of the spectral density (Fig. 5a inset). The axial H-bonding in the revQUBEKit simulation is primarily responsible for this enhancement. In contrast, the higher intensities above 600 cm⁻¹ in the spectral densities from QUBEKit and revQUBEKit (Fig. 5a) lead to larger $\lambda_{\rm HF}$ values than that from QM/MM. As discussed later, the QM/MM chromophore-solvent model may underestimate the coupling between the electronic transition and the high-frequency chromophore vibrational modes due to closer peripheral H-bonding solvent, leading to less intense peaks in the high-frequency region of the spectral density. The total reorganization energies λ , from the force fields are the net result of the lower $\lambda_{\rm LF}$ and the higher $\lambda_{\rm HF}$ compared to the respective values from QM/MM.

TABLE I. Computed reorganization energies of CV^+ in methanol (λ) and the contributions from the low-frequency and high-frequency regions (λ_{LF} and λ_{HF}) in units of eV. The various models for CV^+ (top) include full MM solvation for the energy gap calculations, whereas the different solvent environments (bottom) are all generated from the QM/MM AIMD trajectory.

Different models for CV ⁺ with full MM solvent			
	$\lambda_{ m LF}$	$\lambda_{ m HF}$	λ
QUBEKit	0.011	0.067	0.078
revQUBEKit	0.030	0.073	0.103
QM/MM	0.040	0.050	0.090
Different MM solvent environments with QM CV ⁺			
	$\lambda_{ m LF}$	$\lambda_{ m HF}$	λ
CV ⁺ only	0.006	0.049	0.055
4 Peripheral	0.005	0.047	0.052
1 Axial	0.024	0.052	0.076
4 Axial	0.030	0.053	0.083
Full MM	0.040	0.050	0.090

With the Condon approximation and the second-order cumulant truncation, the absorption spectrum depends solely on the spectral density (Eq. 3). We present the resulting spectra in Figure 5b, with all spectra aligned energetically with the absorption maxima for better comparison of spectral shapes, see SI, section S8 for unaligned spectra and values for applied energy shifts. The maxima from all three trajectories are within 0.07 eV of each other, showing that configurations sampled with the QUBEKit and revQUBEKit FFMD have similar energy gaps as the QM/MM AIMD configurations.

The total absorption spectra, Figure 5b, show that the QUBEKit FFMD leads to the most narrow absorption spectrum, whereas the revQUBEKit FFMD produces a spectrum more similar in width and shape to the spectrum from QM/MM AIMD, but with more intensity in the vibronic tail of the spectrum. These spectra can be further analyzed by separately examining the high and low frequency contributions to the spectra.

The spectra generated from the high-frequency region of the spectral density (above 200 cm⁻¹, Figure 5c) reveals the underlying vibronic structure, with the QUBEKit and revQUBEKit spectra showing more structure due to the increased intensity of the peaks in the high-frequency region of the spectral density above 750 cm⁻¹. The spectra generated from the low-frequency region of the spectral density below 200 cm⁻¹, Figure 5c, correspond to inhomogeneous broadening from the solvent dynamics and show a Gaussian form. Here we can see that the trend in the spectral width parallels both the intensity in the low-frequency region of the spectral density, Figure 5a, and the low-frequency reorganization energy value, with the QUBEKit spectrum being the most narrow, followed by revQUBEKit and then QM/MM spectra. Overall, we can consider the total absorption spectrum as a combination of the low and high-frequency contributions, where we see that QM/MM gives more broadening from the low-frequency contribution due to stronger coupling to the solvent environment, but less broadening from the high-frequency contribution due to weaker vibronic coupling to the chromophore degrees of freedom.

Wondering if 60 ps was long enough time to sample solvent environments and achieve full solvent-induced broadening, we also analyzed the excitation energies of the revQUBEKit trajectory over a longer timescale of 10 ns. The resulting ensemble of excitation energies for the 10 ns trajectory had a nearly identical distribution as that from the 60 ps trajectory with a mean of 3.01 \pm 0.07 eV and 3.02 \pm 0.07 eV respectively (see SI, section S7).

We next turn to the analysis of specific solvent interactions to reveal how these interactions control both the inhomogeneous and vibronic spectral broadening using the QM/MM AIMD trajectory.

C. Effect of specific solvent interactions on spectral lineshapes

In this section we go beyond the bulk solvent description and isolate the effect of specific chromophore-solvent

interactions. To further analyze how the solvent dynamics control the spectral broadening, we compute the spectral density and the corresponding linear absorption spectrum considering different specific solvent environments for the vertical excitation energies with the same QM/MM AIMD trajectory. To isolate the spectral contributions of only the chromophore, we compute the TDDFT vertical excitation energies with all solvent stripped away. To isolate the effect of the strong peripheral H-bonds formed from the CV⁺ amine donor, we include only those four methanol solvent molecules in the MM region of our QM/MM vertical excitation energy calculations, see Figure 1a. We also examine the effect of the solvent interacting with the π -system of the chromophore by including the four methanol solvent molecules closest to CV⁺ within the cylindrical axial region, with one of those solvent molecules forming the axial H-bond with the CV⁺ amine acting as an acceptor that we analyzed previously, see Figure 1b. We also isolate the effect of the single H-bonding axial methanol molecule by including it in the excitation energy calculations as it goes from being 9.0 Å away from the chromophore during the start of the trajectory to being completely H-bonded to the chromophore at the end of the 60 ps. Lastly, we consider the effect of treating the surrounding nearby solvent at the QM level of theory instead of as fixed MM point charges.

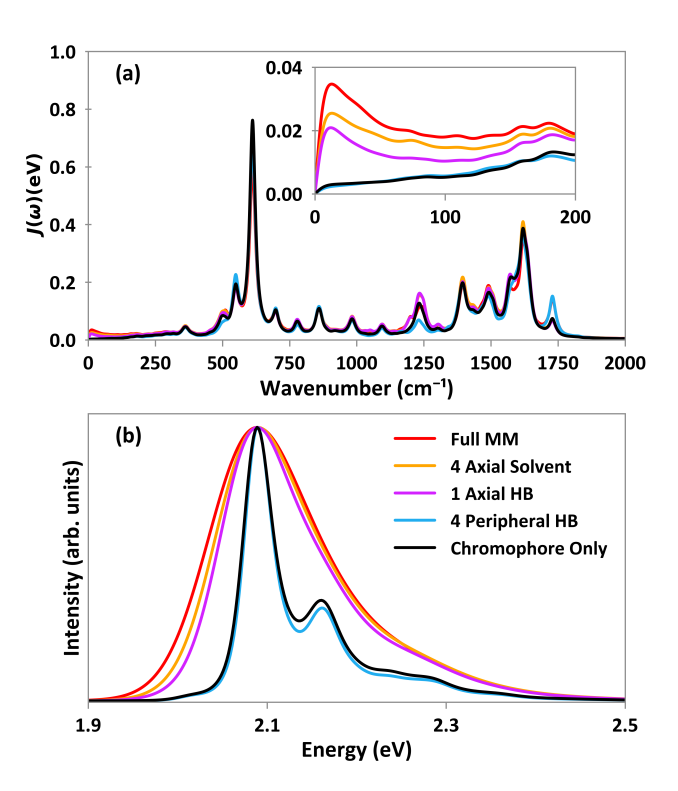


FIG. 6. The computed (a) spectral density and (b) linear absorption spectrum for CV⁺ in methanol for the QM/MM AIMD trajectory with vertical excitation energies computed with different solvent environments. All solvent is treated as MM fixed point charges.

For the various specific chromophore-solvent interactions, the resulting spectral densities and linear absorption spectra are shown in Figure 6. The absorption spectra are once again aligned according to their maxima, with the corresponding unshifted spectra shown in the SI, section S8. In the spectral density in Figure 6a, we see that the chromophore-only snapshots produce low intensity in the low-frequency region, as expected where there is no solvent contribution. The corresponding linear absorption spectrum in Figure 6b shows very little broadening and a clear vibronic shoulder. The addition of the four methanol molecules that form peripheral H-bonds red-shifts the maximum by 0.014 eV (see section S8), but produces very little change in the spectral density or the shape or width of the absorption spectrum compared to the chromophore-only spectrum. In fact, measuring the full-width half-max (FWHM), which for these spectra only encompasses the 0-0 peak and not the vibronic shoulder, the peripheral solvent leads to a smaller value (0.039 eV FWHM) compared to the chromophore only spectrum (0.042 eV FWHM), showing that these strong H-bonds formed with the methanol solvent do not lead to inhomogeneous spectral broadening and in fact make the chromophore slightly more rigid. In contrast, if we replace those four H-bonding methanol solvent molecules with the four closest solvent molecules in the axial region of the chromophore that interact more strongly with the π -system of CV⁺, there is a significant increase in the intensity of the low-frequency region of the spectral density and the absorption spectrum becomes significantly broader (0.137 eV FWHM), nearly as broad as the spectrum with the full MM solvation shell that includes more than 1600 solvent molecules (0.148 eV FWHM). Compared to the spectrum generated from the chromophoreonly snapshots, the spectrum generated with the four axial solvent molecules blue shifts by 0.021 eV, whereas the full MM solvent region blue shifts by 0.030 eV. Including just the one solvent molecule that forms the axial H-bond at ~ 40 ps into the trajectory, we see that the spectral density and the linear absorption spectrum are very similar to those generated with four solvent molecules (0.126 eV FWHM). Upon close approach and formation of the axial H-bond, this one solvent molecule clearly has an immense effect on the spectral broadening.

Examining the corresponding reorganization energies in the bottom part of Table I, we see that the high-frequency reorganization energies, $\lambda_{\rm HF}$, are around 0.05 eV for all MM solvent environments, suggesting that the contribution from the higher-frequency chromophore vibrational degrees of freedom is consistent across all solvent environments. The low-frequency reorganization energy, $\lambda_{\rm LF}$, from the CV⁺ chromophore only without any MM solvent, is only 0.006 eV, reflecting a minimal contribution from chromophore vibrations to the low-frequency spectral density. Including the four peripheral H-bonding solvent molecules barely changes the reorganization energies, indicating that the strong peripheral hydrogen bonds contribute little to the low-frequency

solvent modes for inhomogenous broadening, consistent with the simulated optical spectra. On the other hand, the inclusion of the four axial solvent molecules increases $\lambda_{\rm LF}$ to 0.030 eV, close to the value for full MM solvent (0.040 eV). The λ_{LF} value for the single H-bonding axial solvent molecule is 0.024 eV, close to that from four axial solvent molecules and not far from the total MM solvent λ_{LF} value, showing that a single axial solvent molecule is responsible for well over half of the $\lambda_{\rm LF}$ reorganization energy of a full solvated system. This result once again shows that the low-frequency solvent modes, specifically the motions of the axial solvent molecules that presumably interact strongly with the π -electrons of the chromophore, cause the long-time relaxation of the energy-gap fluctuation and the resulting inhomogeneous broadening in the absorption spectrum. It is well-known that in the slow modulation (inhomogeneous) limit, the Stokes shift, as defined by the difference between absorption and emission maxima, is twice the reorganization energy.²² Therefore, we estimate that the solvent-induced Stokes shift from our QM/MM AIMD simulation would be about $2\lambda_{\rm LF} = 0.080$ eV, not far from the observed experimental Stokes shift of 0.084 eV^{103} or $0.099 \text{ eV}^{63,104}$ for CV⁺ in methanol. Overall, our results demonstrate that it is critical to accurately account for the interactions between the chromophore and the axial solvent molecules in both MD simulations and excited state calculations in order to properly capture solvent-induced inhomogeneous broadening in the spectrum.

An additional source of inhomogeneous broadening is the full polarization of the chromophore-solvent environment. This polarization, along with potential charge transfer, can be achieved by using a QM description of the first solvent shell in the VEE calculations. For the same QM/MM trajectory snapshots, where there is no structural changes of the chromophore or solvent, we computed the vertical excitation energies for both the chromophore and all methanol molecules within 5 Å of the chromophore at the QM level, with the remaining methanol molecules at the MM level ($\approx 230 \text{ QM atoms}$). This QM solvent shell treatment in the excitation energies leads to a shift to lower energies, see SI section S8, and some minor additional inhomogeneous broadening, see Figure 7a. The corresponding spectral density, see SI section S9, shows that this QM treatment of the solvent in the VEE calculations leads to minimal change in the vibronic coupling of the high-frequency chromophore degrees of freedom. Despite the increased broadening with QM treatment of solvent for the VEEs, which is aligned with previous studies, ²⁹ the simulated spectrum based on the QM/MM trajectory produces an absorption spectrum more narrow than experiment.

The $\mathrm{CV^+}$ and methanol QM/MM AIMD configurations presumably have errors due to the QM/MM interface, which affect the interaction of the chromophore and solvent. The MM treatment of solvent during the QM/MM AIMD may lead to over-polarization of the QM region, $^{105-108}$ and therefore closer chromophore-solvent

distances, potentially leading to the weaker vibronic coupling seen in our computed spectral density and high-frequency absorption spectrum. Similar narrowing of the vibronic contribution of the solute vibrations due to explicit solvent has been observed in a previous study, however this narrowing was balanced by a broadening of the spectrum through progressions along solute-solvent vibrations.³⁷

As a test of this narrowing due to explicit MM solvent solvent hypothesis, we computed the Franck-Condon spectrum of CV⁺ in methanol in both frozen MM solvent and frozen QM solvent environments for one frame from the QM/MM trajectory. Note that by treating the solvent as frozen, the solvent modes do not directly contribute to vibronic broadening, but instead only provide an electrostatic and polarization environment for the chromophore solute. We applied an Ohmic implicit solvent broadening parameter to the computed Franck-Condon spectra corresponding to a solvent reorganization energy of $\lambda = 0.001$ a.u., see SI. For computation with a full QM solvent shell, we use the same 5 Å QM solvent shell as in our vertical excitation energy calculations described above (≈ 230 QM atoms). The ground state and excited state geometry of the QM chromophore was optimized and normal modes computed in the field of the fixed solvent. These adiabatic Hessian Franck-Condon spectra show that additional vibronic broadening occurs with the QM treatment of the frozen solvent environment, with the computed Franck-Condon spectrum producing a broader vibronic shoulder than in experiment, see Figure 7b. Note that this additional vibronic broadening must come from the change in the position of the chromophore relative to the solvent associated with the QM treatment of the first solvation shell. The static Franck-Condon spectrum with frozen MM solvent highly resembles the dynamic cumulant spectrum from the QM/MM AIMD trajectory with the excitation energies calculated with MM solvent (comparing the solid red lines in panels (a) and (b) of Fig. 7), showing that the two spectral simulation methods are consistent within this QM/MM model.

To determine which solvent interactions contributed to this vibronic broadening, we then calculated the Franck-Condon spectrum for only the closest four axial solvent molecules as QM or only the four peripheral Hbonding solvent molecules as QM, with all remaining solvent treated as MM. The QM treatment of the axial solvent led to minimal change in the spectrum, see the blue dotted line in Figure 7b. In contrast, the QM treatment of the four peripheral H-bonding solvent molecules (blue dashed line) led to significant additional vibronic broadening, with the spectrum nearing the result for the QM solvation shell treatment (blue solid line). Analyzing the average peripheral H-bond distance between the solvent and the amine of CV⁺ from the optimized structures shows that the H-bond distance increases by 0.12-0.26 Å going from MM to QM treatment of these solvent molecules, see SI section S10. To better understand this

change in distance, we revisit the potential energy scan for a peripheral H-bond, where the methanol molecule was treated as QM, see blue line in Figure 3 (top), and recall that the minimum in the potential of the H-bonding methanol is at a larger distance for QM treatment compared to MM treatment, in agreement with the change in distance for the optimized geometry.

We then attempted to reproduce the same increase in vibronic broadening seen for the QM solvent optimized structures by increasing the van der Waals radii by 0.30 Å for all atoms within the QUBEKit force field. This increase in van der Waals radii was chosen so that optimizing the ground state chromophore geometry within an MM solvent environment produced peripheral H-bond distances similar to those obtained when optimizing within a QM solvent shell (see SI, section S10). Additionally, 0.30 Å is also close to the difference in potential minima between the QM-QM/MM and QUBEKit interaction energies shown in Figure 3. The resulting spectra generated from optimized geometries with the solvent only treated at the MM level remarkably mimic the spectral width of the chromophore optimized with the QM H-bonded solvent. These findings indicate that peripheral H-bonds play an important role in determining the vibronic broadening of CV⁺ in methanol, with an MM treatment of these solvent molecules potentially restricting the motion of the QM chromophore and decreasing vibronic coupling. A QM treatment of the solvent during either the geometry optimization or potentially also during the MD may be essential to producing the correct chromophore-solvent distances and allowing for the full vibronic coupling of the chromophore.

V. CONCLUSIONS

In this work, we went beyond an implicit solvent picture to analyze the chromophore-solvent dynamics and specific chromophore-solvent interactions that contribute to the absorption spectral lineshape and spectral broadening of CV⁺ in methanol. We show that, compared to QM/MM AIMD simulations, molecular dynamics performed with the ab initio parametrized QUBEKit force field does a good job of simulating the chromophore degrees of freedom, but the default procedure of computing partial atomic charges of the chomophore in implicit solvent underestimates the polarization due to explicit solvent that occurs with the QM/MM chromophoresolvent model. Re-parametrizing the force field with charges computed from explicit solvent snapshots improves the chromophore-solvent description, resulting in H-bond formation aligned with what we observe in the QM/MM trajectory.

We here reveal the specific chromophore-solvent interactions that contribute to both inhomogenous and vibronic broadening. Solvent in the axial region of the chromophore interacts with the π -system, leading to substantial inhomogeneous broadening. Our analysis of a

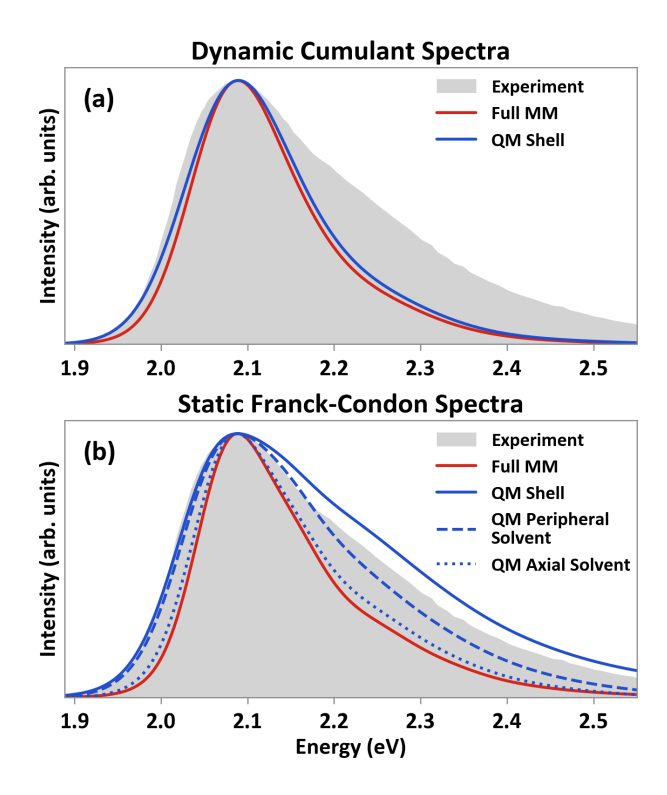


FIG. 7. Absorption spectra for CV^+ in methanol from experiment 103 and computed (a) with the cumulant method using Eqs. 1 - 3 from the QM/MM AIMD trajectory using either all MM solvent or a QM solvent shell surrounded by MM solvent in the TDDFT calculations and (b) for a single snapshot from the AIMD simulation computed with the adiabatic Hessian Franck-Condon method, where the geometry of the QM chromophore is optimized in frozen MM solvent, in a frozen QM solvent shell, with four frozen QM peripheral solvent molecules, or with four frozen QM axial solvent molecules. All QM regions are surrounded by remaining fixed point charge MM solvent.

single axial H-bonded methanol shows that it produces a strong electric-field at the amine site with the O-H bond dipole of methanol aligned with the π -system of the chromophore, and that this one solvent molecule is responsible for the large increase in the spectral width. The methanol molecules that form strong H-bonds peripheral to the chromophore decrease the excitation energy, but do not contribute to inhomogeneous broadening or any increase in the reorganization energy, presumably because they are very stable throughout the dynamics and lead to minimal energy gap fluctuation. However, these peripheral H-bonds likely play a key role in capturing the correct vibronic broadening, as we observe a substantial increase in vibronic spectral width if these methanol molecules are treated with QM during geometry optimization and normal mode computation. Both our potential energy scans along the H-bond and our geometry optimizations in frozen solvent suggest that the MM solvent interfacing with the QM chromophore holds the solvent too close to the chromophore compared to a QM

solvent treatment, which likely restricts the motion of the chromophore atoms leading to a decrease in vibronic coupling. We find that only with the QM treatment of the solvent does the CAM-B3LYP/6-31G(d) spectral shape approach that of experiment.

Additional sources of error could also contribute to the underestimation of the experimental spectral width of CV⁺ in methanol. From our benchmark Franck-Condon calculations in implicit solvent, we know that the LC- ω HPBE functional produces a broader vibronic spectrum than CAM-B3LYP, and it may be that the larger degree of exact exchange is necessary to correctly model the ground and excited state curvature of CV⁺ in methanol. An alternative possible source of error is that a higher lying state is contributing to the experimental absorption spectrum. One of the authors recently explored this nonadiabatic excited state mixing effect for the absorption spectrum of the methylene blue chromophore, finding significant spectral broadening due to nonadiabatic effects from S_1 and S_2 mixing. 109 Although our QM/MM AIMD trajectories show minimal excited state mixing, without excited state calculations at a higher level of theory beyond TDDFT, it is difficult to know the correct excited state behavior for CV⁺, and some experimental results suggest nonadiabatic effects in the strongly coupled vibronic mode. 103,110 Moreover, we account for nuclear quantum effects crudely through a phenomenological quantum correction factor, and more accurate treatments, e.g., using path-integral $\mathrm{MD^{75}}$ or a Wigner distribution, 37,111 may lead to further broadening. Ultimately, higher accuracy will be achieved with the use of QM solvent during the dynamics, which potentially will allow for further coupling to either solvent dynamics or vibronic degrees of freedom.

VI. SUPPORTING INFORMATION

The Supporting Information is available free of charge at [insert website upon publication].

DFT benchmark calculations, GAFF results, MD equilibration, energies of S₁ and S₂ states, electric field analysis, charges, long timescale FFMD simulations, unshifted absorption spectra, QM solvent effects, and Franck-Condon vibronic spectra simulations for explicit solvent configurations. Separate input, force field, and xml files are also included for AMBER and OpenMM.

VII. ACKNOWLEDGEMENTS

The force field parametrization, QM/MM simulations, and optical spectroscopy simulations were supported by NSF Grant No. CHE-1955656. Analysis of specific solvent contributions to spectral shape, partial atomic charges, and H-bond analysis were supported by DOE

BES CPIMS program Grant No. DE-SC0024267. This research used computing resources of the MERCED cluster at UC Merced under NSF Grant No.1429783, and the Pinnacles cluster at UC Merced under NSF Grant No. 2019144. We wish to thank Professor Daniel Cole and group at Newcastle University for assistance with the QUBEKit software.

VIII. REFERENCES

- ¹J. R. Reimers, K. R. Wilson, and E. J. Heller, "Complex time-dependent wave packet technique for thermal equilibrium systems: Electronic spectra," J. Chem. Phys. **79**, 4749–4757 (1983).
- ²J. P. Bergsma, P. H. Berens, K. R. Wilson, D. R. Fredkin, and E. J. Heller, "Electronic spectra from molecular dynamics: a simple approach," The Journal of Physical Chemistry 88, 612–619 (1984), https://doi.org/10.1021/j150647a055.
- ³R. Crespo and M. Barbatti, "Spectrum simulation and decomposition with nuclear ensemble: Formal derivation and application to benzene, furan and 2-phenylfuran," Theo. Chem. Accounts 131 (2012).
- ⁴L. I. T. S. L. F. R. da S. Junior Luiz Antonio Ribeiro de Sousa Junior Rafael Timoteo and da Silva Filho Demetrio A., "A dft study of a set of natural dyes for organic electronics," Journal of Molecular Modeling **23**, 343 (2017).
- ⁵E. U. Condon, "A theory of intensity distribution in band systems," Phys. Rev. 28, 1182–1201 (1926).
- E. U. Condon, "Nuclear motions associated with electron transitions in diatomic molecules," Phys. Rev. 32, 858–872 (1928).
 E. G. Dymond and J. Franck, "Elementary processes of photochemical reactions," Trans. Faraday Soc. 21, 536–542 (1926).
- ⁸A. Toniolo and M. Persico, "Efficient calculation of franck-condon factors and vibronic couplings in polyatomics," Journal of Computational Chemistry 22, 968–975 (2001).
- ⁹F. Santoro, R. Improta, A. Lami, J. Bloino, and V. Barone, "Effective method to compute franck-condon integrals for optical spectra of large molecules in solution," The Journal of Chemical Physics 126, 084509 (2007).
- ¹⁰D. W. Silverstein and L. Jensen, "Vibronic coupling simulations for linear and nonlinear optical processes: Theory," The Journal of Chemical Physics 136, 064111 (2012).
- ¹¹R. Gherib, S. N. Genin, and I. G. Ryabinkin, "On the importance of well-defined thermal correlation functions in simulating vibronic spectra," The Journal of Physical Chemistry A 126, 3947–3956 (2022).
- ¹² J. Cerezo, F. J. Avila Ferrer, G. Prampolini, and F. Santoro, "Modeling solvent broadening on the vibronic spectra of a series of coumarin dyes. from implicit to explicit solvent models," Journal of Chemical Theory and Computation 11, 5810–5825 (2015).
- ¹³S. Budzak, A. D. Laurent, C. Laurence, M. Medved, and D. Jacquemin, "Solvatochromic shifts in uv-vis absorption spectra: The challenging case of 4-nitropyridine n-oxide," Journal of Chemical Theory and Computation 12, 1919–1929 (2016).
- ¹⁴D. Loco, S. Jurinovich, L. Cupellini, M. F. S. J. Menger, and B. Mennucci, "The modeling of the absorption lineshape for embedded molecules through a polarizable QM/MM approach," Photochem. Photobiol. Sci. 17, 552–560 (2018).
- ¹⁵L. O. Kostjukova, S. V. Leontieva, and V. V. Kostjukov, "The vibronic absorption spectra and electronic states of proflavine in aqueous solution," Computational and Theoretical Chemistry 1197, 113144 (2021).
- ¹⁶C. Zhu, "Franck-condon factors within damped displacement harmonic oscillators: Solvent-enhanced absorption and fluores-

cence spectra," Journal of the Chinese Chemical Society **70**, 219–231 (2022).

¹⁷T. J. Zuehlsdorff and C. M. Isborn, "Combining the ensemble and franck-condon approaches for calculating spectral shapes of molecules in solution," J. Chem. Phys. **148**, 024110 (2018).

¹⁸T. J. Zuehlsdorff, A. Montoya-Castillo, J. A. Napoli, T. E. Markland, and C. M. Isborn, "Optical spectra in the condensed phase: Capturing anharmonic and vibronic features using dynamic and static approaches," J. Chem. Phys **151**, 074111 (2019).

¹⁹S. V. Shedge, T. J. Zuehlsdorff, A. Khanna, S. Conley, and C. M. Isborn, "Explicit environmental and vibronic effects in simulations of linear and nonlinear optical spectroscopy," The Journal of Chemical Physics 154, 084116 (2021), https://pubs.aip.org/aip/jcp/article-pdf/doi/10.1063/5.0038196/15588081/084116_1_online.pdf.

²⁰T. J. Zuehlsdorff, S. V. Shedge, S.-Y. Lu, H. Hong, V. P. Aguirre, L. Shi, and C. M. Isborn, "Vibronic and environmental effects in simulations of optical spectroscopy," Annual Review of Physical Chemistry 72, 165–188 (2021), pMID: 33395546, https://doi.org/10.1146/annurev-physchem-090419-051350.

²¹ J. Cerezo, D. Aranda, F. J. Avila Ferrer, G. Prampolini, and F. Santoro, "Adiabatic-molecular dynamics generalized vertical hessian approach: A mixed quantum classical method to compute electronic spectra of flexible molecules in the condensed phase," Journal of Chemical Theory and Computation 16, 1215–1231 (2020), pMID: 31855424, https://doi.org/10.1021/acs.jctc.9b01009.

²²S. Mukamel, Principles of Nonlinear Optical Spectroscopy (Oxford University Press, New York, 1995).

²³M. C. Zwier, J. M. Shorb, and B. P. Krueger, "Hybrid molecular dynamics-quantum mechanics simulations of solute spectral properties in the condensed phase: Evaluation of simulation parameters," Journal of Computational Chemistry 28, 1572–1581 (2007), https://onlinelibrary.wiley.com/doi/pdf/10.1002/jcc.20662.

²⁴A. M. Rosnik and C. Curutchet, "Theoretical characterization of the spectral density of the water-soluble chlorophyll-binding protein from combined quantum mechanics/molecular mechanics molecular dynamics simulations," Journal of Chemical Theory and Computation 11, 5826–5837 (2015), pMID: 26610205, https://doi.org/10.1021/acs.jctc.5b00891.

²⁵S. Chandrasekaran, M. Aghtar, S. Valleau, A. Aspuru-Guzik, and U. Kleinekathöfer, "Influence of force fields and quantum chemistry approach on spectral densities of bchl a in solution and in fmo proteins," The Journal of Physical Chemistry B 119, 9995–10004 (2015), pMID: 26156758, https://doi.org/10.1021/acs.jpcb.5b03654.

²⁶M. K. Lee and D. F. Coker, "Modeling electronic-nuclear interactions for excitation energy transfer processes in light-harvesting complexes," The Journal of Physical Chemistry Letters 7, 3171–3178 (2016), pMID: 27472379, https://doi.org/10.1021/acs.jpclett.6b01440.

²⁷D. Loco and L. Cupellini, "Modeling the absorption lineshape of embedded systems from molecular dynamics: A tutorial review," Int. J. Quantum Chem. 119, e25726 (2018).

²⁸F. Segatta, L. Cupellini, M. Garavelli, and B. Mennucci, "Quantum chemical modeling of the photoin-duced activity of multichromophoric biosystems," Chemical Reviews 119, 9361–9380 (2019), pMID: 31276384, https://doi.org/10.1021/acs.chemrev.9b00135.

²⁹T. J. Zuehlsdorff, H. Hong, L. Shi, and C. M. Isborn, "Influence of Electronic Polarization on the Spectral Density," J. Phys. Chem. B **124**, 531–543 (2020).

³⁰T. Zuehlsdorff, H. Hong, L. Shi, and C. Isborn, "Nonlinear spectroscopy in the condensed phase: The role of duschinsky rotations and third order cumulant contributions," J. Chem. Phys. 153, 044127–16 (2020).

³¹M. Bondanza, L. Cupellini, F. Lipparini, and B. Mennucci, "The multiple roles of the protein in the photoactivation of orange carotenoid protein," Chem 6, 187-203 (2020).

³²M. S. Chen, Y. Mao, A. Snider, P. Gupta, A. Montoya-Castillo, T. J. Zuehlsdorff, C. M. Isborn, and T. E. Markland, "Elucidating the role of hydrogen bonding in the optical spectroscopy of the solvated green fluorescent protein chromophore: Using machine learning to establish the importance of high-level electronic structure," The Journal of Physical Chemistry Letters 14, 6610–6619 (2023), pMID: 37459252, https://doi.org/10.1021/acs.jpclett.3c01444.

³³G.-J. Han, Zhao and K.-L. "Effects hydrobonding photochemistry: gen on tuning Concerted hydrogen-bond strengthening and weakening,' ChemPhysChem 9, 1842–1846 (2008), https://chemistryeurope.onlinelibrary.wiley.com/doi/pdf/10.1002/cphc.200800371.

³⁴P. Song and F.-C. Ma, "Intermolecular hydrogen-bonding effects on photophysics and photochemistry," International Reviews in Physical Chemistry 32, 589–609 (2013), https://doi.org/10.1080/0144235X.2013.811891.

³⁵M. P. Kabir, Y. Orozco-Gonzalez, G. Hastings, and S. Gozem, "The effect of hydrogen-bonding on flavin's infrared absorption spectrum," Spectrochimica Acta Part A: Molecular and Biomolecular Spectroscopy 262, 120110 (2021).

³⁶D. P. N. Le, G. Hastings, and S. Gozem, "How aqueous solvation impacts the frequencies and intensities of infrared absorption bands in flavin: The quest for a suitable solvent model," Molecules 29 (2024), 10.3390/molecules29020520.

³⁷A. Petrone, J. Cerezo, F. J. A. Ferrer, G. Donati, R. Improta, N. Rega, and F. Santoro, "Absorption and emission spectral shapes of a prototype dye in water by combining classical/dynamical and quantum/static approaches," The Journal of Physical Chemistry A 119, 5426–5438 (2015), pMID: 25699575, https://doi.org/10.1021/jp510838m.

³⁸S.-Y. Lu, T. J. Zuehlsdorff, H. Hong, V. P. Aguirre, C. M. Isborn, and L. Shi, "The influence of electronic polarization on nonlinear optical spectroscopy," J. Phys. Chem. B **125**, 12214–12227 (2021).

³⁹C. M. Isborn, A. W. Götz, M. A. Clark, R. C. Walker, and T. J. Martínez, "Electronic absorption spectra from MM and ab initio QM/MM molecular dynamics: environmental effects on the absorption spectrum of photoactive yellow Protein," J. Chem. Theory Comput. 8, 5092–5106 (2012).

⁴⁰C. M. Isborn, B. D. Mar, B. F. E. Curchod, I. Tavernelli, and T. J. Martínez, "The charge transfer problem in density functional theory calculations of aqueously solvated molecules," The Journal of Physical Chemistry B 117, 12189–12201 (2013), pMID: 23964865, https://doi.org/10.1021/jp4058274.

⁴¹M. R. Provorse, T. Peev, C. Xiong, and C. M. Isborn, "Convergence of excitation energies in mixed quantum and classical solvent: Comparison of continuum and point charge models," The Journal of Physical Chemistry B 120, 12148–12159 (2016).

⁴²O. Andreussi, I. G. Prandi, M. Campetella, G. Prampolini, and B. Mennucci, "Classical force fields tailored for qm applications: Is it really a feasible strategy?" Journal of Chemical Theory and Computation 13, 4636–4648 (2017), pMID: 28910099, https://doi.org/10.1021/acs.jctc.7b00777.

⁴³I. Cacelli and G. Prampolini, "Parametrization and validation of intramolecular force fields derived from dft calculations," Journal of Chemical Theory and Computation 3, 1803–1817 (2007), pMID: 26627623, https://doi.org/10.1021/ct700113h.

⁴⁴T. Verstraelen, D. Van Neck, P. W. Ayers, V. Van Speybroeck, and M. Waroquier, "The gradient curves method: An improved strategy for the derivation of molecular mechanics valence force fields from ab initio data," Journal of Chemical Theory and Computation 3, 1420–1434 (2007), pMID: 26633214, https://doi.org/10.1021/ct6002093.

⁴⁵ J. G. McDaniel and J. R. Schmidt, "First-principles many-body force fields from the gas phase to liquid: A "universal" approach," The Journal of Physical Chemistry B 118, 8042–8053 (2014), pMID: 24655231, https://doi.org/10.1021/jp501128w.

⁴⁶S. Grimme, "A general quantum mechanically derived force field (qmdff) for molecules and condensed phase simulations," Journal of Chemical Theory and Computation 10, 4497–4514 (2014), pMID: 26588146, https://doi.org/10.1021/ct500573f.

⁴⁷L. Vanduyfhuys, S. Vandenbrande, T. Verstraelen, R. Schmid, M. Waroquier, and V. Van Speybroeck, "Quickff: A program for a quick and easy derivation of force fields for metal-organic frameworks from ab initio input," Journal of Computational Chemistry 36, 1015–1027 (2015), https://onlinelibrary.wiley.com/doi/pdf/10.1002/jcc.23877.

⁴⁸J.-P. Piquemal and K. D. Jordan, "Preface: Special Topic: From Quantum Mechanics Force Fields," The Journal ofChemical Physics 147. https://pubs.aip.org/aip/jcp/article-161401 (2017),pdf/doi/10.1063/1.5008887/15534564/161401_1_online.pdf.

⁴⁹G. König and S. Riniker, "On the faithfulness of molecular mechanics representations of proteins towards quantum-mechanical energy surfaces," Interface Focus 10, 20190121 (2020), https://royalsocietypublishing.org/doi/pdf/10.1098/rsfs.2019.0121.

- ⁵⁰ J. G. Vilhena, L. Greff da Silveira, P. R. Livotto, I. Cacelli, and G. Prampolini, "Automated parameterization of quantum mechanically derived force fields for soft materials and complex fluids: Development and validation," Journal of Chemical Theory and Computation 17, 4449–4464 (2021), pMID: 34185536, https://doi.org/10.1021/acs.jctc.1c00213.
- ⁵¹G. Prampolini, L. Greff da Silveira, J. G. Vilhena, and P. R. Livotto, "Predicting spontaneous orientational selfassembly: In silico design of materials with quantum mechanically derived force fields," The Journal of Physical Chemistry Letters 13, 243–250 (2022), pMID: 34968058, https://doi.org/10.1021/acs.jpclett.1c03517.
- ⁵²K.-S. Csizi and M. Reiher, "Universal qm/mm approaches for general nanoscale applications," WIREs Computational Molecular Science 13, e1656 (2023), https://wires.onlinelibrary.wiley.com/doi/pdf/10.1002/wcms.1656.

⁵³ J. T. Horton, A. E. A. Allen, L. S. Dodda, and D. J. Cole, "QUBEKit: Automating the Derivation of Force Field Parameters from Quantum Mechanics," **59**, 1366–1381 (2019).

- ⁵⁴C. Ringrose, J. T. Horton, L.-P. Wang, and D. J. Cole, "Exploration and validation of force field design protocols through qm-to-mm mapping," Phys. Chem. Chem. Phys. **24**, 17014–17027 (2022).
- ⁵⁵E. Vogel, A. Gbureck, and W. Kiefer, "Vibrational spectroscopic studies on the dyes cresyl violet and coumarin 152," Journal of Molecular Structure 550-551, 177–190 (2000).
- ⁵⁶S. J. Isak and E. M. Eyring, "Cresyl violet chemistry and photophysics in various solvents and micelles," Photochem. Photobiol. A: Chem. **64**, 343–358 (1992).
- ⁵⁷G. B. Dutt, S. Doraiswamy, N. Periasamy, and B. Venkataraman, "Rotational reorientation dynamics of polar dye molecular probes by picosecond laser spectroscopic technique," The Journal of Chemical Physics 93, 8498–8513 (1990), https://pubs.aip.org/aip/jcp/articlepdf/93/12/8498/11227458/8498_1_online.pdf.
- ⁵⁸D. I. Kreller and P. V. Kamat, "Photochemistry of sensitizing dyes: spectroscopic and redox properties of cresyl violet," J. Phys. Chem. **95**, 4406–4410 (1991).
- ⁵⁹W. Leng and A. M. Kelley, "Resonance Raman intensity analysis of cresyl violet bound to SiO 2 colloidal nanoparticles," Langmuir 19, 7049-7055 (2003).
- ⁶⁰A. Jafari, A. Ghanadzadeh, H. Tajalli, M. Yeganeh, and M. Moghadam, "Electronic absorption spectra of cresyl violet acetate in anisotropic and isotropic solvents," Spectrochimica Acta Part A: Molecular and Biomolecular Spectroscopy 66, 717–725 (2007).
- ⁶¹E. Beuerman, N. S. Makarov, M. Drobizhev, and A. Rebane, "Justification of two-level approximation for description of twophoton absorption in oxazine dyes," in *Organic Photonic Mate*rials and *Devices XII*, Vol. 7599, edited by R. L. Nelson, F. Kajzar, and T. Kaino, International Society for Optics and Pho-

- tonics (SPIE, 2010) p. 75990X.
- ⁶²D. A. Steinhurst and J. C. Owrutsky, "Second harmonic generation from oxazine dyes at the air/water interface," The Journal of Physical Chemistry B 105, 3062–3072 (2001), https://doi.org/10.1021/jp003893q.
- ⁶³ J. Lu, Y. Lee, and J. M. Anna, The Journal of Physical Chemistry B **124**, 8857–8867 (2020).
- ⁶⁴V. V. Kostjukov, "Photoexcitation of cresyl violet dye in aqueous solution: TD-DFT study," Theoretical Chemistry Accounts 140, 1–12 (2021).
- ⁶⁵L. Allan and T. J. Zuehlsdorff, "Taming the third order cumulant approximation to linear optical spectroscopy," The Journal of Chemical Physics 160, 074108 (2024), https://pubs.aip.org/aip/jcp/article-pdf/doi/10.1063/5.0182745/19687707/074108_1_5.0182745.pdf.
- ⁶⁶J. S. Bader and B. J. Berne, "Quantum and classical relaxation rates from classical simulations," J. Chem. Phys. **100**, 8359 (1994).
- ⁶⁷S. A. Egorov, K. F. Everitt, and J. L. Skinner, "Quantum Dynamics and Vibrational Relaxation," J. Phys. Chem. A **103**, 9494–9499 (1999).
- ⁶⁸H. Kim and P. J. Rossky, "Evaluation of Quantum Correlation Functions from Classical Data," J. Phys. Chem. B **106**, 8240 (2002).
- ⁶⁹C. P. Lawrence and J. L. Skinner, "Quantum corrections in vibrational and electronic condensed phase spectroscopy: Line shapes and echoes," Proceedings of the National Academy of Sciences 102, 6720–6725 (2005).
- ⁷⁰S. Valleau, A. Eisfeld, and A. Aspuru-Guzik, "On the alternatives for bath correlators and spectral densities from mixed quantum-classical simulations," J. Chem. Phys. **137**, 224103 (2012)
- ⁷¹A. Damjanović, I. Kosztin, U. Kleinekathöfer, and K. Schulten, "Excitons in a photosynthetic light-harvesting system: A combined molecular dynamics, quantum chemistry, and polaron model study," Physical Review E 65, 031919–24 (2002), 0107064.
- ⁷²C. Olbrich, J. Strümpfer, K. Schulten, and U. Kleinekathöfer, "Theory and Simulation of the Environmental Effects on FMO Electronic Transitions," J. Phys. Chem. Lett. **14**, 1771–1776 (2011).
- ⁷³S. Jurinovich, L. Viani, I. G. Prandi, T. Renger, and B. Mennucci, "Towards an ab initio description of the optical spectra of light-harvesting antennae: application to the CP29 complex of photosystem II," Phys. Chem. Chem. Phys. 17, 14405–14416 (2015).
- ⁷⁴M. K. Lee, P. Huo, and D. F. Coker, "Semiclassical Path Integral Dynamics: Photosynthetic Energy Transfer with Realistic Environment Interactions," Annu. Rev. Phys. Chem. **67**, 639–668 (2016).
- ⁷⁵T. J. Zuehlsdorff, J. A. Napoli, J. M. Milanese, T. E. Markland, and C. M. Isborn, "Unraveling electronic absorption spectra using nuclear quantum effects: photoactive yellow protein and green fluorescent protein chromophores in water," J. Chem. Phys. 149, 024107 (2018).
- ⁷⁶R. Scholz, L. Gisslén, B.-E. Schuster, M. B. Casu, T. Chassé, U. Heinemeyer, and F. Schreiber, "Resonant Raman spectra of diindenoperylene thin films," The Journal of Chemical Physics 134, 014504 (2011).
- ⁷⁷A. P. Shreve and R. A. Mathies, "Thermal Effects in Resonance Raman Scattering: Analysis of the Raman Intensities of Rhodopsin and of the Time-Resolved Raman Scattering of Bacteriorhodopsin," J. Phys. Chem. 99, 7285–7299 (1995).
- ⁷⁸F. Markel, N. S. Ferris, I. R. Gould, and A. B. Myers, "Mode-specific vibrational reorganization energies accompanying photoinduced electron transfer in the hexamethyl-benzene/tetracyanoethylene charge-transfer complex," J. Am. Chem. Soc. 114, 6208–6219 (1992).
- ⁷⁹J. B. Page and D. L. Tonks, "On the separation of resonance Raman scattering into orders in the time correlator theory," The

Journal of Chemical Physics 75, 5694–5708 (1981).

⁸⁰A. Charaf-Eddin, A. Planchat, B. Mennucci, C. Adamo, and D. Jacquemin, "Choosing a functional for computing absorption and fluorescence band shapes with td-dft," Journal of Chemical Theory and Computation 9, 2749–2760 (2013), pMID: $26583866,\, https://doi.org/10.1021/ct4000795.$

⁸¹F. J. Avila Ferrer, J. Cerezo, E. Stendardo, R. Improta, and F. Santoro, "Insights for an accurate comparison of computational data to experimental absorption and emission spectra: Beyond the vertical transition approximation," Journal of Chemical Theory and Computation 9, 2072–2082 (2013), pMID: 26583553, https://doi.org/10.1021/ct301107m.

 $^{82}\mathrm{T.}$ A. Manz and N. Gabaldon Limas, "Chargemol program for performing ddec analysis,".

⁸³T. A. Manz and N. G. Limas, "Introducing ddec6 atomic population analysis: part 1. charge partitioning theory and methodology," RSC Advances 6, 47771-47801 (2016).

⁸⁴E. Vauthey, K. Holliday, C. Wei, A. Renn, and U. P. Wild, "Stark effect and spectral hole-burning: solvation of organic dyes in polymers," Chemical Physics 171, 253–263 (1993).

⁸⁵U. C. Singh and P. A. Kollman, "An approach to computing electrostatic charges for molecules," Journal of Computational Chemistry 5, 129–145 (1984).

 $^{86}\mathrm{E.}$ Sigfridsson and U. Ryde, "Comparison of methods for deriving atomic charges from the electrostatic potential and moments," Journal of Computational Chemistry 19, 377-395 (1998).

⁸⁷D. Jacquemin, T. L. Bahers, C. Adamo, and I. Ciofini, "What is the "best" atomic charge model to describe through-space charge-transfer excitations?" Phys. Chem. Chem. Phys. 14, 5383-5388 (2012).

⁸⁸D. J. Cole, J. Z. Vilseck, J. Tirado-Rives, M. C. Payne, and W. L. Jorgensen, "Biomolecular Force Field Parameterization via Atoms-in-Molecule Electron Density Partitioning," J. Chem. Theory Comput. 12, 2312-2323 (2016).

⁸⁹M. R. Shirts, C. Klein, J. M. Swails, J. Yin, M. K. Gilson, D. L. Mobley, D. A. Case, and E. D. Zhong, "Lessons learned from comparing molecular dynamics engines on the sampl5 dataset," Journal of Computer-Aided Molecular Design 31, 147-161 (2016).

⁹⁰J. Wang, R. M. Wolf, J. W. Caldwell, P. A. Kollman, and D. A. Case, "Development and testing of a general Amber force field," Journal of Computational Chemistry 25, 1157–1174 (2004).

⁹¹D. A. Case, H. M. Aktulga, K. Belfon, D. S. Cerutti, G. A. Cisneros, V. W. D. Cruzeiro, N. Forouzesh, T. J. Giese, A. W. Götz, H. Gohlke, S. Izadi, K. Kasavajhala, M. C. Kaymak, E. King, T. Kurtzman, T.-S. Lee, P. Li, J. Liu, T. Luchko, R. Luo, M. Manathunga, M. R. Machado, H. M. Nguyen, K. A. O'Hearn, A. V. Onufriev, F. Pan, S. Pantano, R. Qi, A. Rahnamoun, A. Risheh, S. Schott-Verdugo, A. Shajan, J. Swails, J. Wang, H. Wei, X. Wu, Y. Wu, S. Zhang, S. Zhao, Q. Zhu, T. E. Cheatham, D. R. Roe, A. Roitberg, C. Simmerling, D. M. York, M. C. Nagan, and K. M. Merz, "Ambertools," Journal of Chemical Information and Modeling 63, 6183–6191 (2023).

⁹²D. Case, K. Belfon, I. Ben-Shalom, S. Brozell, D. Cerutti, T. Cheatham, III, V. Cruzeiro, T. Darden, R. Duke, G. Giambasu, M. Gilson, H. Gohlke, A. Goetz, R. Harris, S. Izadi, S. Izmailov, K. Kasavajhala, A. Kovalenko, R. Krasny, T. Kurtzman, T. Lee, S. LeGrand, P. Li, C. Lin, J. Liu, T. Luchko, R. Luo, V. Man, K. Merz, Y. Miao, O. Mikhailovskii, G. Monard, H. Nguyen, A. Onufriev, F. Pan, S. Pantano, R. Qi, D. Roe, A. Roitberg, C. Sagui, S. Schott-Verdugo, J. Shen, C. Simmerling, N. Skrynnikov, J. Smith, J. Swails, R. Walker, J. Wang, L. Wilson, R. Wolf, X. Wu, Y. Xiong, Y. Xue, and D. York, "Amber 2020,"

⁹³B. Leimkuhler and C. Matthews, "Rational Construction of Stochastic Numerical Methods for Molecular Sampling," Applied Mathematics Research eXpress 34-56 (2012),https://academic.oup.com/amrx/articlepdf/2013/1/34/397230/abs010.pdf.

⁹⁴T. Schlick, Molecular Modeling and Simulation: An Interdisciplinary Guide: An Interdisciplinary Guide (Springer New York, 2010).

⁹⁵H. J. C. Berendsen, J. P. M. Postma, W. F. van Gunsteren, A. DiNola, and J. R. Haak, "Molecular dynamics with coupling to an external bath," The Journal of Chemical Physics 81, 3684-3690 (1984).

⁹⁶P. Eastman, J. Swails, J. D. Chodera, R. T. McGibbon, Y. Zhao, K. A. Beauchamp, L.-P. Wang, A. C. Simmonett, M. P. Harrigan, C. D. Stern, R. P. Wiewiora, B. R. Brooks, and V. S. Pande, "OpenMM 7: Rapid development of high performance algorithms for molecular dynamics," 13, e1005659.

⁹⁷Z. Zhang, X. Liu, K. Yan, M. E. Tuckerman, and J. Liu, "Unified efficient thermostat scheme for the canonical ensemble with holonomic or isokinetic constraints via molecular dynamics," The Journal of Physical Chemistry A 123, 6056–6079 (2019).

 $^{98}\mathrm{S}.$ Hirata and M. Head-Gordon, "Time-dependent density functional theory within the Tamm-Dancoff approximation," Chem. Phys. Lett. **314**, 291–299 (1999).

⁹⁹C. M. Isborn, N. Luehr, I. S. Ufimtsev, and T. J. Martínez, "Excited-state electronic structure with configuration interaction singles and Tamm-Dancoff time-dependent density functional theory on graphical processing Units," J. Chem. Theory Comput. 7, 1814–1823 (2011).

 $^{100}\mathrm{S}.$ Seritan, C. Bannwarth, B. S. Fales, E. G. Hohenstein, C. M. Isborn, S. I. L. Kokkila-Schumacher, X. Li, F. Liu, N. Luehr, J. W. Snyder Jr., and et al, "Terachem: A graphical processing unit-accelerated electronic structure package for large-scale ab initio molecular dynamics," WIREs Computational Molecular Science 11, e1494 (2021).

 $^{101}\mathrm{T.}$ J. Zuehlsdorff, "Molspeckpy: Spectroscopy python code," .

 $^{102}\mathrm{C}.$ Fitz patrick, J. H. Odhner, and R. J. Levis, "Spectral signatures of ground- and excited-state wavepacket interference after impulsive excitation," The Journal of Physical Chemistry A 124, 6856-6866 (2020), pMID: 32786657, https://doi.org/10.1021/acs.jpca.0c03912.

¹⁰³J. Brazard, L. A. Bizimana, T. Gellen, W. P. Carbery, and D. B. Turner, "Experimental detection of branching at a conical intersection in a highly fluorescent molecule," The Journal of Physical Chemistry Letters 7, 14-19 (2016), pMID: 26647278, https://doi.org/10.1021/acs.jpclett.5b02476.

¹⁰⁴S. R. Rather and G. D. Scholes, "Slow Intramolecular Vibrational Relaxation Leads to Long-Lived Excited-State Wavepack-

ets," J. Phys. Chem. A 120, 6792-6799 (2016).

¹⁰⁵D. Das, K. P. Eurenius, E. M. Billings, P. Sherwood, D. C. Chatfield, M. Hodošček, and B. R. Brooks, "Optimization of quantum mechanical molecular mechanical partitioning schemes: Gaussian delocalization of molecular mechanical charges and the double link atom method," The Journal of Chemical Physics 117, 10534-10547 (2002), https://pubs.aip.org/aip/jcp/articlepdf/117/23/10534/19236300/10534_1_online.pdf.

¹⁰⁶P. Amara and M. J. Field, "Evaluation of an ab initio quantum mechanical/molecular mechanical hybrid-potential linkatom method," Theoretical Chemistry Accounts 109, 43-52

(2003).

 $^{107}\mathrm{H}.$ Μ. Senn and W. Thiel, "Qm/mm methods systems," Chemie biomolecular Angewandte for International Edition 48. 1198 - 1229(2009).https://onlinelibrary.wiley.com/doi/pdf/10.1002/anie.200802019.

 $^{108}{
m J}.$ Dziedzic, Т. Head-Gordon, M. Head-Gordon, Skylaris, and C.-K. "Mutually polarizable QM/MM optimized model with in situ localized basis functions," The Journal of Chemical **Physics** 074103 (2019),https://pubs.aip.org/aip/jcp/articlepdf/doi/10.1063/1.5080384/15554809/074103_1_online.pdf.

 $^{109}\mathrm{A.~J.}$ Dunnett, D. Gowland, C. M. Isborn, A. W. Chin, and T. J. Zuehlsdorff, "Influence of non-adiabatic effects on linear absorption spectra in the condensed phase: Methylene blue,"

Journal of Chemical Physics **155**, 144112 (2021).

- ¹¹⁰M. S. Barclay, J. S. Huff, R. D. Pensack, P. H. Davis, W. B. Knowlton, B. Yurke, J. C. Dean, P. C. Arpin, and D. B. Turner, "Characterizing mode anharmonicity and huang-rhys factors using models of femtosecond coherence spectra," The Journal of Physical Chemistry Letters 13, 5413–5423 (2022),
- pMID: 35679146, https://doi.org/10.1021/acs.jpclett.1c04162.
 ¹¹¹J. Cerezo, F. Santoro, and G. Prampolini, en "Comparing classical approaches with empirical or quantum-mechanically derived force fields for the simulation electronic lineshapes: application to coumarin dyes," Theor Chem Acc 135, 143 (2016).